

# Direct index of refraction measurement at extreme ultraviolet wavelength region with a novel interferometer

Chang Chang<sup>1,2</sup>, Erik Anderson<sup>1</sup>, Patrick Naulleau<sup>1</sup>, Eric Gullikson<sup>1</sup>, Kenneth Goldberg<sup>1</sup>, David Attwood<sup>1,2</sup>

<sup>1</sup>Center for X-Ray Optics,  
Lawrence Berkeley National Laboratory, Berkeley, CA 94720

<sup>2</sup>Department of Electrical Engineering & Computer Sciences,  
University of California, Berkeley, CA 94720

*cncchang@lbl.gov*

The first direct measurement of the dispersive part of the refractive index is performed at extreme ultraviolet (EUV) wavelengths, where absorption is higher as compared with hard x-ray and visible wavelengths. A novel diffractive optical element, which combines the functions of a grating and a zoneplate, is fabricated following Fourier optical techniques and employed here for the first time at EUV/soft x-ray wavelengths. Both the real and imaginary parts of the complex refractive indices are measured directly by this technique without recourse to Kramers-Kronig transformations. Data for Al and Ni, in the vicinity of their L and M-edges, respectively, are presented as first examples of this technique. ©2001 Optical Society of America

**OCIS codes:** 160.2120, 120.3180

## 1. Introduction

Refractive indices,  $n(\omega) = 1 - \delta(\omega) + i\beta(\omega)$ , in the extreme ultraviolet (EUV) wavelength region are complex, highly absorptive and have strong wavelength (photon energy) dependence.<sup>1</sup>

The absorptive part  $\beta(\omega)$  of the refractive index at EUV wavelengths is well-tabulated by photo-absorption measurements. However, the real (dispersive) part of the refractive index  $\delta(\omega)$  at EUV wavelengths is less accurately known. Interferometry, which can provide independent measurements of  $\delta$  and  $\beta$ , is difficult in the EUV/Soft X-Ray(SXR) regions due to high absorption by the many atomic resonances and the lack of high optical quality beam-splitters. Joyeux *et. al.*<sup>2</sup> have had some success using an interferometer based on a bi-mirror reflective splitter, but were limited by the trade-off between throughput and spectral resolution. Bonse and Hart<sup>3</sup> have been successful at significantly higher photon energies, where  $\beta/\delta \ll 1$ , using crystal diffraction techniques. Presently in the EUV/SXR region, knowledge of  $\delta$  is determined either indirectly from a Kramers-Kronig transformation of the imaginary (absorptive) part,  $\beta(\omega)$ ,<sup>4-7</sup> or by least-square fitting Fresnel coefficients obtained from reflectance measurements.<sup>7-9</sup> Neither of these methods provide an independent measurement of  $\delta(\omega)$ . The  $\delta(\omega)$  values obtained from the Kramers-Kronig relationship depend entirely on the  $\beta(\omega)$  values. Because the Kramers-Kronig relationship requires a wide range of spectrum of  $\beta(\omega)$  to obtain each point  $\delta(\omega)$  on the spectrum, errors in  $\beta(\omega)$ , especially near absorption edges, affect the accuracy of the resultant  $\delta(\omega)$  values. The accuracy of  $\delta(\omega)$  values determined from reflectance experiments are sensitive to surface roughness, chemistry and contamination, and to the fact that the accuracy of this fitting depends strongly on  $\beta/\delta$ , working well only for energies with  $\beta/\delta \ll 1$ .

Here, we present an amplitude-division transmission interferometer that can be used to measure both the dispersive and the absorptive parts of the refractive index independently by determining the phase-shift and the visibility of interferograms. Because the determination of  $\delta$  directly from the phase-shift is independent of  $\beta$ , this interferometer can measure  $\delta$  across the absorption edges without being affected by sharp spectral variations of the  $\beta$  value. In addition, the sample is probed in transmission at normal incidence in this interferometer, thus, it is less sensitive to errors associated with surface roughness, chemistry and contamination, as compared with reflectance measurements, assuming that the thickness of the sample is much greater than that of the surface layer.

## 2. Interferometer

The interferometer used for the measurements presented here is shown conceptually in Fig. 1. The size of the pinhole,  $5\mu m$ , is chosen to be smaller than the coherence area of the beam,<sup>12</sup> guaranteeing spatially coherent illumination of the interferometer. In concept, the pinhole-diffracted beam then

propagates through a binary transmission grating, which serves as a beam-splitter, followed by a zoneplate lens used to focus the beams to the sample plane. As actually used, the grating and zoneplate are combined for improved efficiency into a single diffractive element. This combined optical element provides two side-by-side focal spots of equal intensity is discussed shortly, following Eq.(1).

The sample mask, consisting of side-by-side window pairs, is placed at the back focal plane of the zoneplate. The window pairs consist of two  $5\mu m \times 5\mu m$  cross-sectioned openings. Reference window pairs are free of test material, while other pairs have one window coated with test material. In taking data, we first align a reference window pair to the two side-by-side first order focal beam spots and record a reference interferogram. We then move the sample mask to illuminate a window pair in which one side contains test material, and record the test interferogram. By introducing the test material into one arm of the interferometer, the fringes of the interferogram shift due to the refractive properties of the material, essentially a path integration of  $\delta(\omega)$ . Additionally, the visibility of the interferogram is reduced due to absorption. The interferograms are recorded on a back-thinned EUV-sensitive CCD camera. The complex index of refraction is determined by comparing these two interferograms for fringe-shift and visibility change, which are directly related to  $\delta$  and  $\beta$ , respectively.

A Fourier transform method<sup>12,15</sup> is used to extract both the phase-shift and visibility from the interferograms. The extracted values are averaged over the full area of the interference pattern. The phase shift,  $\phi$ , is simply the difference between the two independently reconstructed phase maps from the interferograms. The value of  $\delta$  is determined by  $\phi = \frac{2\pi}{\lambda} t \delta$ , where  $\lambda$  is the wavelength and  $t$  is the thickness of the sample.

The relative optical intensity of the two beams, after propagating through the sample mask, is related to observed visibility of the interferogram by  $V = \frac{2\sqrt{\alpha}}{1+\alpha}$ , where  $\alpha$  is the relative intensity after propagating through the sample. From the relative intensity  $\alpha$ , the value of  $\beta$  is obtained by  $\alpha = \exp\{-\frac{4\pi}{\lambda}\beta t\}$ .

#### **A. Novel diffractive optical element**

The use of two sequential diffractive elements (the grating and zoneplate), each of which has a theoretical efficiency to first order of  $1/\pi^2$ , limits the overall efficiency of the interferometer. This efficiency can be significantly improved by consolidating the functionality of the grating and the zoneplate into a single diffractive optical element. This is done by combining the binary grating

and zoneplate through a bit-wise XOR operation.<sup>13</sup>

The two optical elements used in this XOR pattern, a 50% duty-cycle binary amplitude grating of period  $d$ , and a 50% duty-cycle binary amplitude zoneplate of diameter  $D$  and outermost zone-width  $\Delta r$ , can be represented by  $G(x, y) = \frac{1}{2}[1 + \text{sgn}(\cos \frac{2\pi x}{d})]$  and  $ZP(x, y) = \frac{1}{2}[1 + \text{sgn}(\cos \frac{\pi(x^2+y^2)}{\Delta r(D-\Delta r)})]$ , respectively.<sup>14</sup> Expanding these two patterns in their respective Fourier series and noting that the XOR pattern of the grating and zoneplate can be expressed as  $XOR(x, y) = G(x, y) + ZP(x, y) - 2G(x, y)ZP(x, y)$ , we have

$$XOR(x, y) = \frac{1}{2} - 2 \left[ \sum_{\substack{m=-\infty \\ m \neq 0}}^{\infty} \frac{\sin(m\pi/2)}{m\pi} e^{-i\frac{2m\pi x}{d}} \right] \left[ \sum_{\substack{n=-\infty \\ n \neq 0}}^{\infty} \frac{\sin(n\pi/2)}{n\pi} e^{-i\frac{n\pi(x^2+y^2)}{\Delta r(D-\Delta r)}} \right]. \quad (1)$$

Examining the first order terms in both the grating and zoneplate, i.e.  $(m, n) = (\pm 1, 1)$ , its efficiency is given by the square of its coefficient  $[2(1/\pi)(1/\pi)]^2 = 4/\pi^4$ , which is a factor of 4 increase in optical throughput as compared with separate grating and zoneplate. Since the membranes on which these optical elements are fabricated have finite absorption, there is an additional gain of efficiency due to the fact that only one membrane is required.

This combined diffractive element, when illuminated by a uniform wavefront, has the interesting property that it produces two symmetric off-axis focal spots,  $(m, n) = (\pm 1, 1)$ , at the back focal plane of the zoneplate. This can be seen by multiplying the two exponentials in Eq.(1) and completing the square for  $x$ -terms. The separation of these two beam spots is determined by  $\Delta x \approx 2 \sin^{-1}(\lambda/d) \frac{\Delta r D}{\lambda} = 2\Delta r D/d$ . Note that this separation is independent of wavelength  $\lambda$ . Thus as the wavelength is varied for spectral determinations of  $\delta$  and  $\beta$ , the focal length (distance from the XOR pattern to the sample mask) varies, but the lateral separation of the two beam spots remains fixed. Therefore, the index of refraction as a function of wavelength can be obtained simply by translating the sample mask along the optical axis.

### 3. Experimental setup

This experiment is performed at undulator beamline 12.0 of the Advanced Light Source, a third generation synchrotron radiation facility.<sup>11</sup> Undulator radiation provides the required EUV photon flux and, with pinhole spatial filtering, the spatial coherence required for the interferometric experiments. The beamline monochromator provides a spectral resolution  $\lambda/\Delta\lambda = 1100$ . As described above, a single XOR diffractive element combining a grating ( $d = 16\mu\text{m}$ ) and zoneplate ( $D = 400\mu\text{m}$ ,  $\Delta r = 0.2\mu\text{m}$ ) is used for optimum efficiency. This new diffractive element is fabricated using electron beam patterning and nanofabrication techniques.<sup>16</sup> The separation of the two

beam spots at the back focal plane is  $\Delta x = 10\mu m$ .

The sample mask is also fabricated by electron beam lithography on a  $100nm$  thick silicon nitride membrane. The thickness of the  $Si_3N_4$  membrane is relatively uniform over the  $10\mu m$  separation of the two beam spots. The sample is prepared with the test material being evaporated onto the nitride membrane. The thickness of the test material is measured both by a profilometer and a spectral reflectivity system to an accuracy  $\pm 1nm$ .

## 4. Experimental results

### A. Aluminum across its L-edge

Measured  $\delta$  and  $\beta$  values for aluminum  $67.0 \pm 0.1nm$  thick are shown in Figs. 2 in blue. The results obtained with this interferometer resolve the fine aluminum  $L$  - edge structure, i.e. the  $L_3$  edge at 72.7 eV and the  $L_2$  edge at 73.1 eV, in both  $\delta$  and  $\beta$ . Moreover, it is also evident that the shapes of the  $\delta$  and  $\beta$  curves, though determined independently, are closely related. The sharpest increase in  $\beta$  occurs at 72.7 eV which coincides exactly with the dip of the  $\delta$  curve at the  $L_3$  edge. Furthermore, the sharp increase of  $\beta$  at 73.1 eV also coincides exactly with the dip of the  $\delta$  curve at the  $L_2$  edge. For comparison, the best available data for aluminum refractive indices is shown in red,<sup>18</sup> where the  $\delta$  value is obtained by Kramers-Kronig transformations of  $\beta$  values over a wide spectrum.

### B. Nickel across its M-edge

Measured  $\delta$  and  $\beta$  values for nickel of thickness  $20.6 \pm 0.1nm$  are shown in Figs. 3. The Nickel  $M_3$  edge at 66.2eV is clearly resolved and the  $\delta$  and  $\beta$  values at this edge are seen to be closely correlated. The error-bars for the nickel data are slightly larger than that of the aluminum data, mainly because of the lower photon flux available in our experiment at the nickel M-absorption-edge. Thus, longer exposure times were required resulting in greater noise due to vibration. Improved accuracy at the absorption edge will require increased system stability or increased optical throughput. The best available refractive index values of nickel<sup>17</sup> are shown in red for comparison.

## 5. Conclusion

The first direct measurement of the dispersive part of the index of refraction at EUV wavelengths is performed using interferometry. A new diffractive optical element based on Fourier optical techniques is, for the first time, designed, fabricated, and employed in the interferometer for improved efficiency. This interferometer directly measures  $\delta$  values at wavelengths where it is desired. No

compilation of  $\beta$  values over a wide spectral range is needed. As a first example,  $\delta$  and  $\beta$  values of aluminum and nickel are obtained by this interferometer at wavelengths close to their atomic resonances, i.e. Al L-edge and Ni M-edge. Extensions of these studies to additional materials (Si, Mo,...), and to shorter wavelengths (1 to 5  $nm$ ) in the soft x-ray spectral region are planned

## References

1. D. T. Attwood, *Soft x-rays and extreme ultraviolet radiation : principles and applications*, (Cambridge University Press, 1999).
2. D. Joyeux, F. Polack, D. Phalippou, “An interferometric determination of the refractive part of optical constants for carbon and silver across soft X-ray absorption edges”, *Rev. Sci. Instrum.*, **70**, 2921-6 (1999).
3. U. Bonse, M. Hart, “An X-ray interferometer”, *Appl. Phys. Lett.*, **6**, 155 (1965).
4. H. Ehrenreich, H.R. Philipp “Optical properties of Ag and Cu”, *Phys. Rev.*, **128**, 1622-9 (1962).
5. H.-J. Hagemann, W. Gudat, C. Kunz, “Optical constants from the far infrared to the X-ray region: Mg, Al, Cu, Ag, Au, Bi, C, and  $Al_2O_3$ ”, *J. Opt. Soc. Am.*, **65**, 742-4 (1975).
6. E. Shiles, T. Sasaki, M. Inokuti, D. Y. Smith “Self-consistency and sum-rule tests in the Kramers-Kronig analysis of optical data: Applications to aluminum”, *Phys. Rev. B*, **22**, 1612-28 (1980).
7. R. Soufli, Ph.D. Thesis, Univ. of California at Berkeley, EECS Dept., “Optical constants of materials in the EUV/Soft X-ray region for multilayer mirror applications.” (1997).
8. W. R. Hunter, “Errors in using the reflectance vs angle of incidence method for measuring optical constants”, *J. Opt. Soc. Am.*, **55**(10), 1197-1204 (1965).
9. W.R. Hunter, “Measurement of optical properties of materials in the vacuum ultraviolet spectral region”, *Appl. Opt.*, **21**, 2103-14 (1982).
10. J. Svatos, D. Joyeux, D. Phalippou, F. Polack, “soft X-ray interferometer for measuring the refractive index of materials”, *Opt. Lett.*, **18**, 1367-9 (1993).
11. D.T. Attwood, P. Naulleau, K.A. Goldberg, E. Tejnil, C. Chang, R. Beguiristain, P. Batson, J. Bokor, E.M. Gullikson, M. Koike, H. Medeck, J.H. Underwood, “Tunable coherent radiation in the soft X-ray

and extreme ultraviolet spectral regions”, *IEEE J. Quantum Electron.*, **35**, 709-20 (1999).

12. C. Chang, P. Naulleau, E. Anderson, D. Attwood, “Spatial coherence characterization of undulator radiation”, *Opt. Commun.*, **182**, 25-34 (2000).
13. The XOR pattern is obtained by first pixelize the binary grating and zoneplate. Each pixel is either 1 or 0 for transmission and absorption, respectively. The two pixelized patterns are then overlapped and compared pixel by pixel to produce the resulting “XOR” pattern, i.e. at each pixel position, if the pixel values of the grating and zoneplate are the same (both 0’s or both 1’s), the value of the corresponding pixel on the “XOR” pattern is 0. Otherwise, the value of the corresponding pixel on the “XOR” pattern is 1.
14. J. W. Goodman, *Introduction to Fourier optics*, 2nd ed., (McGraw-Hill, New York, 1996).
15. M. Takeda, H. Ina, S. Kobayashi, “Fourier-transform method of fringe-pattern analysis for computer-based topography and interferometry”, *J. Opt. Soc. Am.*, **72**, 156-60 (1982).
16. E.H. Anderson, D.L. Olynick, B. Harteneck, E. Veklerov, G. Denbeaux, W. Chao, A. Lucero, L. Johnson, D. Attwood, “Nanofabrication and diffractive optics for high-resolution X-ray applications”, *J. Vac. Sci. Technol. B*, **18**, 2970-5 (2000).
17. E. Gullikson, interactive x-ray refractive indices database, Center for X-Ray Optics, Lawrence Berkeley National Laboratory, [http://www-cxro.lbl.gov/optical\\_constants/](http://www-cxro.lbl.gov/optical_constants/)
18. D.Y. Smith, E. Shiles, M. Inokuti, “The optical properties of metallic aluminum”, in *Handbook of optical constants of solids*, Editor E. Palik, (Academic Press, 1998).



## List of figures

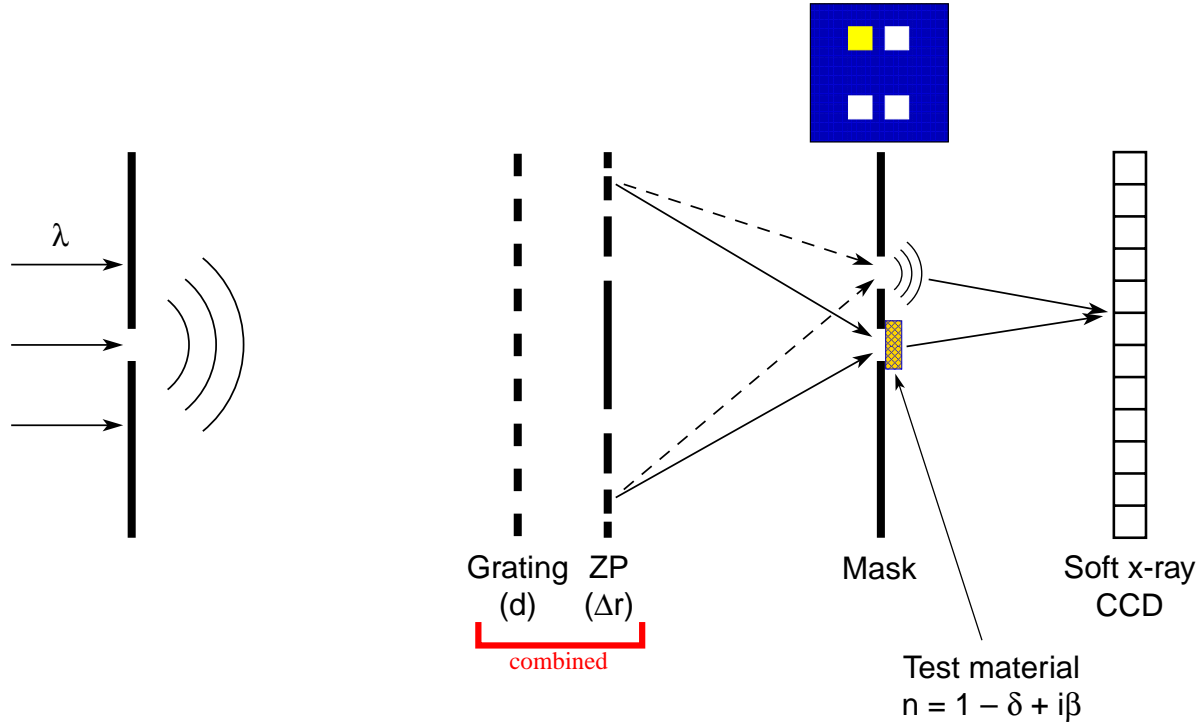


Fig. 1. Experimental Setup: A  $5\mu m$  pinhole is placed at the focus of the beamline optics to provide spatially coherent illumination for this interferometer. The grating serves as the beam splitter which effectively creates orders of virtual sources out of the pinhole. The zoneplate then images the pinhole, together with all the virtual sources created by the grating, to the plane of the sample mask. This mask consists of two  $5\mu m \times 5\mu m$  windows allowing only the zeroth and the first order spots to pass. The test material is then shuffled in and out over one of the windows and a back-thinned EUV-sensitive CCD camera records the respective interferograms for comparison. The functions of the grating and zoneplate have been combined into a single diffractive element following the use of Fourier optical techniques and nanofabrication.

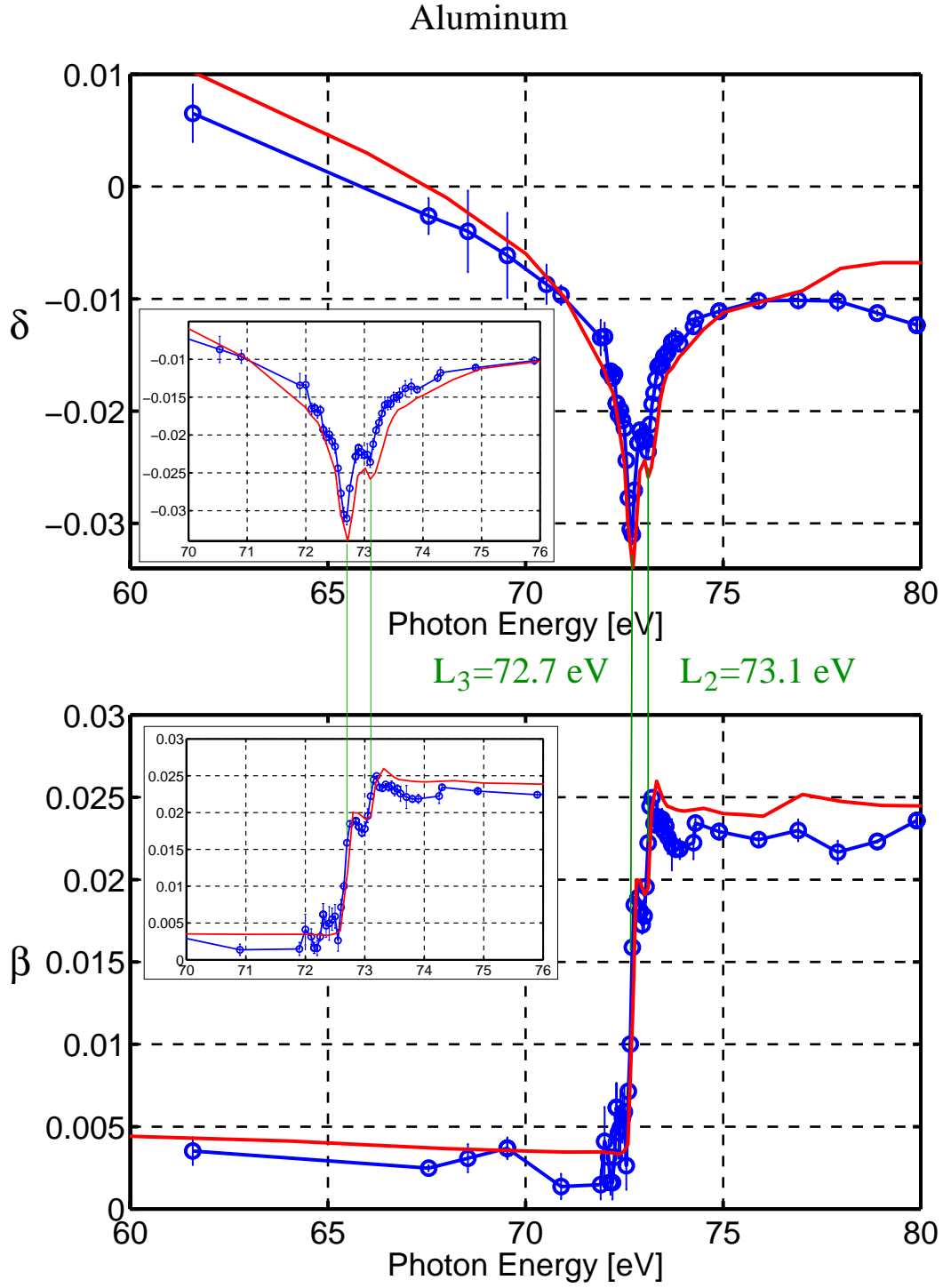


Fig. 2. The experimental results are shown in blue. It is evident that the aluminum L-edge is resolved both in  $\delta$  and  $\beta$  where the position of the  $L_2$  and  $L_3$  edges are 73.1 eV and 72.7 eV, respectively. Note that the values of  $\delta$  and  $\beta$  are obtained directly (independently) from phase shift and visibility change, respectively. The  $\delta$  and  $\beta$  values from Ref.<sup>18</sup> (in red) is derived from Kramers-Kronig transformation of a compilation of absorption and reflectance data. The two data sets agree fairly well both in  $\delta$  and  $\beta$ .

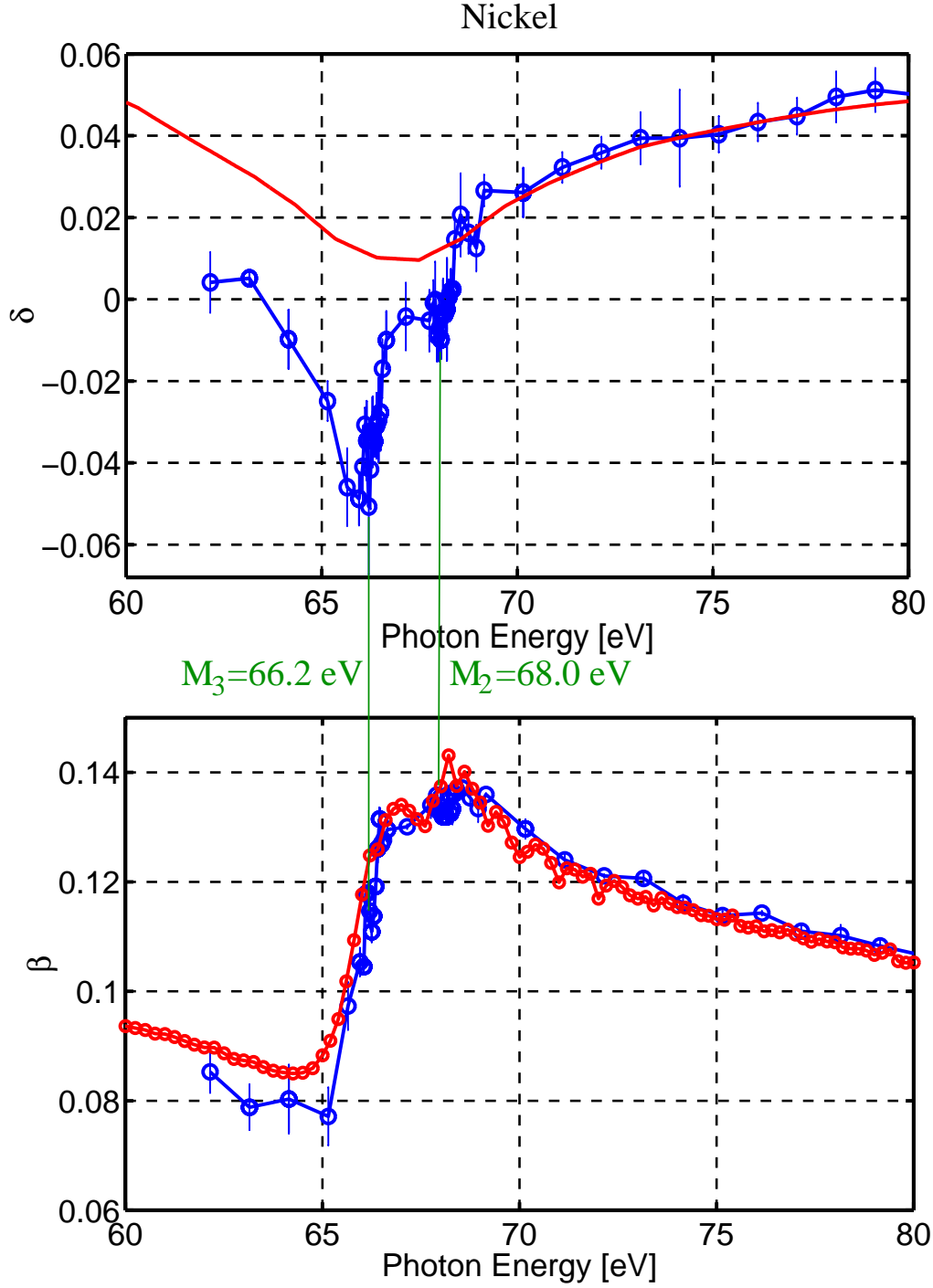


Fig. 3. Nickel: The experimental results are shown in blue. The  $M_3$  edge at  $66.2\text{eV}$  is clearly resolved and the  $\delta$  and  $\beta$  values at this edge are seen to be closely correlated. The typical exposure time ( $\sim 200\text{sec}$ ) for the nickel interferograms is approximately 10 times longer than that of aluminum due to lower beamline flux at low energy. The stages in the experimental setup drift over longer exposure time, thus causing larger error bars in the nickel data. For comparison, current standard nickel refractive indices are shown in red.